Journal of Magnetism and Magnetic Materials xx (2023) xx

Contents lists available at ScienceDirect

Journal of Magnetism and Magnetic Materials

journal homepage: www.elsevier.com/locate/addlet

Material Engineering of 3D-Printed Silicon Steel Alloys for the Next Generation of Electrical Machines and Sustainable Electromobility

Ahmed Selema [a,b,*], Margherita Beretta [a,c], Mohamed N. Ibrahim [a,b], Jo Verwimp [d], Marleen Rombouts [d], Jozef Vleugels [c], Leo A.I. Kestens [a,b], Peter Sergeant [a,b]

[a] Department of Electromechanical, Systems, and Metal Engineering, Ghent University, 9000 Ghent, Belgium
[b] FlandersMake@UGent, Core Lab MIRO, 3001 Leuven, Belgium
[c] Department of Materials Engineering, KU Leuven, Kasteelpark Arenberg 44, 3001 Heverlee, Belgium
[d] Flemish Institute for Technological Research - VITO, Boeretang 200, 2400 , Mol, Belgium

ARTICLE INFO

Keywords:
Additive manufacturing
Electrical machines
3D printed Fe-Si
Magnetic material

ABSTRACT

Recently, there has been a growing need for sustainable and efficient electromobility. Also, the interest in highly-flexible resource-saving production has been increasing. To this aim, standardized manufacturing of electrified powertrains is being replaced by scalable production solutions. With this being said, additive manufacturing (AM) technology through its unmatched flexibility, can be used to manufacture the next generation of electrical machines. One of the main challenges of the existing electrical machines is that the stator and rotor are manufactured only using 2D electrical steel laminations without any design freedom for the third dimension. This research is targeting 3D printing of high quality magnetic materials. Multiple AM technologies allow industrialization of unconventional solutions and different chemical compositions of magnetic material powders can be customized for a wide range of applications including transportation electrification. This study is focusing on 3D micro extrusion technology of highly viscous silicon steel (FeSi) powder pastes. Different soft magnetic cores are printed with different silicon contents. The magnetic BH characteristics and losses of the cores are measured and compared and the best Si content with a higher limitation for eddy current losses is identified. Finally, advanced shape-profiled cores are printed and characterized to evaluate their magnetic properties in comparison to the standard electrical steel. The findings indicate that the utilization of a 3D printed core successfully mitigates eddy current losses within the high-frequency range, while also offering the added benefit of constructing intricate structures.

1. Introduction

Nowadays, the transition to electric vehicles is placing new demands on more flexible manufacturing processes and is driving a change in traditional automotive production. This will have a great impact on manufacturers as well as suppliers. The processes of manufacturing an E-vehicle with an electric drivetrain are fundamentally different from those of a traditional combustion engine. Also, using environmentally friendly and efficient electromobility will be the key differentiator towards zero-emissions and highly automated economies. An electric powertrain is a set of components that convert electric power to mechanical torque to move the vehicle. These components include active parts such as stator, rotor, copper windings, and permanent magnets (PM), with other passive parts such as housing, bearing, insulation, gearbox, etc. An example is demonstrated in **Fig. 1** [1]. The optimization of the E-motor active components results in high power density, compactness, high efficiency and low rare earth PMs and copper content.

The magnetic material laminations typically possess at least 50% of the total weight of the electrical machine including the housing [2]. With the increasing requirements for high efficiency and power density, manufacturability of E-motors gets more complex. Traditional manufacturing methods have much lower flexibility and limited material options. The rise of additive manufacturing (AM) methods provide a more flexible alternative with good reproducibility and better materials engineering.

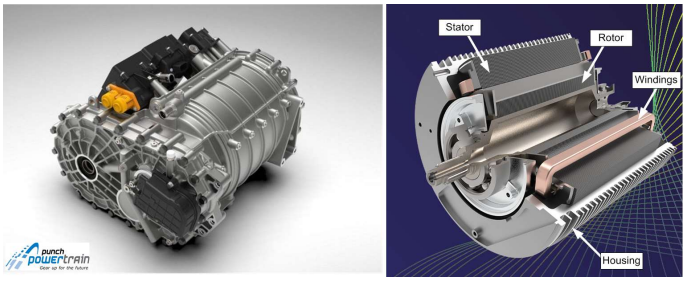

Fig. 1. Main components of an electric powertrain system [1] (Credit: Punch Powertrain NV).

Soft magnetic cores are an essential part inside electrical machines. Bad selection of material or design can result in overweight, high losses, or over-temperature. Electrical steel laminations have been the standard

* Corresponding author.
E-mail addresses: ahmed.selema@ugent.be , selema@ieee.org.

https://doi.org/10.1016/xxxxxxxxxxxxx
Received xx July 2022; Received in revised form xx 2022

choice for the stator and rotor. The major challenge of conventional steel laminations is that it is manufactured and stacked in a 2D plain. The third dimension is not fully utilized. So, manufacturing a non-conventional electric motor such as an axial flux machine will require higher cost and longer fabrication time [3]. Additive manufacturing, however, can be used for building complex shapes that cannot be realized using conventional methods. Besides, AM can also be used for material optimization to minimized weight and magnetic losses [4,5].

In this paper, soft magnetic materials are manufactured using 3D printing technology. With a particular focus on micro extrusion, two different cores are printed with different silicon contents of 3 wt% and 6 wt% Si. The magnetic BH characteristics and losses of the cores are measured and the best Si content with a have higher limitation for eddy current losses is identified. The results are compared with that of a conventional electrical steel under the same frequency level. The paper is divided as follows. Section 2 is introducing the state-of-the-art with respect to additive manufacturing of soft magnetic materials, with different examples illustrating the latest advancement in this field. Different materials are highlighted and their chemical composition is compared. In Section 3, the magnetic measurement calculations are outlined, and the material building and preparation is discussed. Section 4 addresses the material characterization. The core losses are measured and the results are modelled to obtain the fitting parameters for the finite element simulation. In Section 5, advanced shape-profiled cores are printed and measured to assess their properties compared to the standard magnetic materials. Section 6 is devoted to the conclusions and findings.

2. Additive Manufacturing of Magnetic Materials

Additive manufacturing (AM) technologies are known for fast prototyping of a wide variety of complex and scalable shapes. However, the use of AM for building electromagnetic parts (e.g. coils or cores) is still limited [6–9]. AM offers new opportunities for printing soft magnetic materials with improved properties. Different compositions can be printed with a larger electrical resistivity, an increased permeability, and close-to-zero magnetostriction.

A lot of AM technologies are nowadays being used to improve the functionality of materials in terms of magnetic properties as well as physical and mechanical behavior [10]. This includes Electron Beam Melting (EBM) [11], laser powder bed fusion (L-PBF) [12], and 3D micro-extrusion (MEX), also known as robocasting [13]. L-PBF technology can boost the development of custom-shape components. Moreover, material optimization can also be achieved using L-PBF to reduce raw material consumption. 3D micro-extrusion has a unique advantage of multi-material printing which cannot be easily realized using other technologies. In [14], using a multi0nozzle printer, silicon steel (Fe-Si) powder is printed simultaneously with a ceramic insulation to significantly reduce eddy current losses significantly.

In [15,16], using highly viscous pastes, different electromagnetic devices are extruded layer by layer through a nozzle using multi-materials, as shown in **Fig. 2**. With the superior thermal conductivity of the ceramics, the temperature of the test samples can reach up to 300°C.

Numerous research studies have focused on improving the magnetic properties of printed materials. Stornelli conducted a comparative analysis of the magnetic properties of FeSi produced through additive manufacturing, varying the silicon content. They found that the steel containing 6.7wt% of silicon exhibited lower eddy current loss compared to Fe3wt%Si [17]. In another study by Goll [18], extensive research was conducted to explore the potential of enhancing the magnetic properties of electrical steel components using Laser Powder Bed Fusion (LPBF). This was achieved by utilizing electrical steel powder with a silicon content of 6.7wt%, employing topologically optimized designs and/or multi-layered materials in combination with an electrical insulator. In a different study [19], layered structures of Fe6.7%Si were fabricated using LPBF, followed by immersion in a ceramic slurry to create an insulator surface layer.

Soft magnetic materials with high magnetic properties are used to build a rotor for a synchronous reluctance machine with a complex design [20]. In [21], the effect of the powder characteristics on structural and mechanical properties is investigated using additively manufactured Zr-based bulk metallic glass alloys. In [22], different magnetic materials are compared for soft and hard magnetic cores. In [23], L-PBF of complex-shaped soft-magnetic materials is introduced using a Fe-Si-Cr-B-C-based alloy which is very suitable for electric motor rotors. In [24], improved soft magnetic materials with small scale are proposed for power electronics and motor controllers.

In [25], an axial flux machine stator is printed additively using 6.5% silicon steel and SLM technique. The stator was prototyped as one single continuous part with Hilbert space filling pattern. **Fig. 3** shows the stator design, and the white arrows show flux paths along the teeth and yoke. The results demonstrate that the Hilbert structure is effective in reducing the eddy current losses, and it has comparable core losses to ultra-thin gauge laminations. Yet, in this design, the presence of the yoke will result in lower power density compared to a yokeless structure. All the aforementioned examples highlight the importance of AM technology and soft magnetic materials in different industrial sectors.

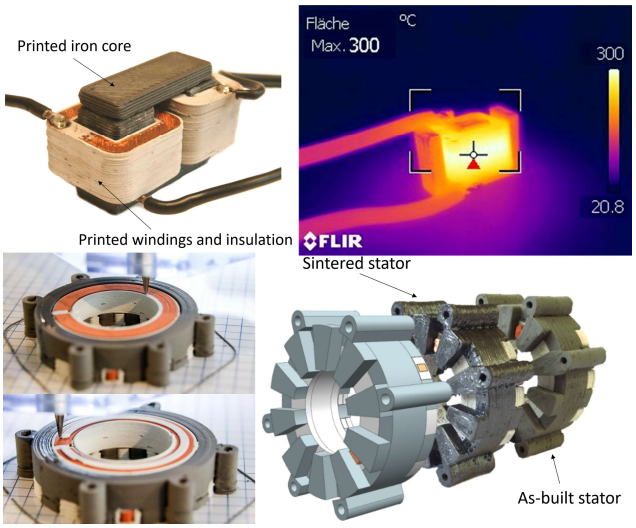

Fig. 2. Multi-material printing of soft magnetic material with copper conductors and ceramic insulation [15].

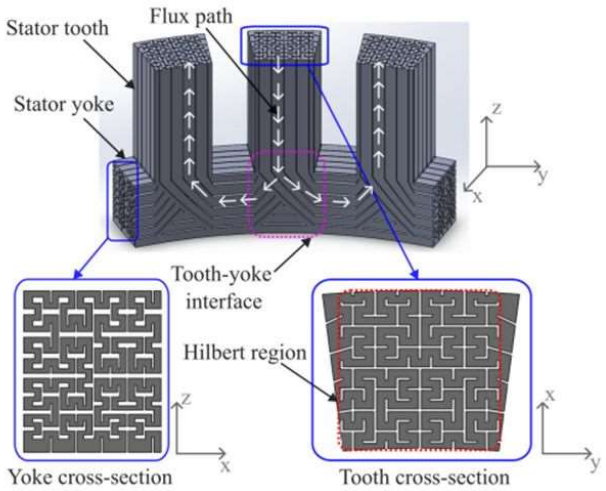

Fig. 3. AM axial flux switched reluctance machine using single material 3D printing [25].

The standard range of metal powder includes a wide variety of soft magnetic alloys to be used in the different AM technologies. **Table 1** summarizes the chemical composition of different soft magnetic alloys [26].

Table 1. Chemical composition of different soft magnetic alloys (nominal wt%) [26].

Alloy	Fe	C	Mn	Si	Cr	Mo	S	P	Co	Ni	Other
430L	Bal.	≤0.03	≤1.0	≤1.0*	17	–	≤0.03	≤0.04	–	–	–
Fe8Cr	Bal.	≤0.03	0.6	0.8	8	0.35	≤0.03	≤0.03	–	–	–
Fe12Cr	Bal.	≤0.03	0.6	0.8	12	0.35	≤0.03	≤0.03	–	–	–
Fe18Cr	Bal.	≤0.03	0.6	0.8	18	0.35	≤0.03	≤0.03	–	–	–
Fe1.5Si	Bal.	≤0.03	≤0.3	1.5	–	–	≤0.03	≤0.03	–	–	–
Fe3Si	Bal.	≤0.03	≤0.3	3	–	–	≤0.03	≤0.03	–	–	–
Fe6Si	Bal.	≤0.03	≤0.3	6	–	–	≤0.03	≤0.03	–	–	–
Fe27Co0.2Si	Bal.	≤0.01	≤0.25	≤0.25	≤0.7	–	≤0.03	≤0.03	27	≤0.7	–
Fe35Co0.2Si	Bal.	≤0.01	≤0.25	≤0.25	≤0.7	–	≤0.03	≤0.03	35	≤0.7	–
Fe49Co2V	Bal.	≤0.05	≤1.0	≤1.0	–	–	≤0.010	≤0.015	49	–	V 2.0
Fe50Co0.2Si	Bal.	≤0.01	≤0.25	≤0.25	≤0.7	–	≤0.03	≤0.03	50	≤0.7	–
Fe50Ni	Bal.	≤0.05	≤0.5	≤0.5	≤0.5	–	≤0.03	≤0.03	–	50	–
Fe80Ni5Mo	Bal.	–	≤0.5	≤0.5	–	5	≤0.03	≤0.03	–	80	–

Fe-Ni alloys typically contain 50 wt% or 80 wt% nickel. This material has lower core losses and is a good choice when a high magnetic permeability is needed. Fe-Ni alloys are also a good choice for resolvers and rotating electrical equipment and demanding applications. Fe-Ni alloy laminations are more expensive and fragile than silicon steel and require special measures during the annealing process to achieve the desired properties and maintain quality. For the best results, manufactures expose the alloy to a dry hydrogen atmosphere and add surface insulation (aluminum oxide and magnesium oxide) during the heat treatment process when the alloy is exposed to temperatures greater than 1090°C [27].

Fe-Co alloys are an appropriate choice when other materials do not meet performance or quality requirements or when applications require high flux densities without saturation. Accordingly, Fe-Co alloys are good for weight-sensitive applications that require less metal to carry the flux. Fe-Co based alloys also have better magnetic characteristics and considerably better performing compared to Fe-Si. With the reduced crystalline anisotropy and magnetostriction, the cobalt content can be optimized for different applications. To give an idea, Fe50Co, has a saturation magnetization of 2.45 T which is the highest value of all magnetic materials [28]. Adding 2% vanadium improves machinability, and increases electrical resistivity, thus reducing the core losses due to eddy currents, without impacting the magnetic properties. The main issue of cobalt is that it has a negative environmental impact and Co-based materials have been classified as having a mutagenic, carcinogenic and reproductive toxicity by the European Registration, Evaluation, Authorization and Restriction of Chemical Substances Program (REACH) [29]. Waste generated from mining and production of cobalt can pollute water, air and soil, leading to decreased crop yields, contaminated food and water, and respiratory and reproductive health issues [30].

Apart from soft magnetic material, AM technology can also be used to print hard magnetic materials for PMs. **Table 2** summarizes different approaches and techniques used to print different alloys of hard magnetic material. The findings reveal that NdFeB exhibits noteworthy magnetic properties, particularly when printed using the Binder Jetting (BjT) method, as long as the maximum processing temperature remains below 150°C. Conversely, it is evident that using the Fused Filament Fabrication (FFF) approach to print the same material results in significantly lower remanence and coercivity.

Table 2. Properties of different hard magnetic materials printed using various AM methods.

Material	AM Methods	Remanence Br (G)	Coercivity Hci (A/m)	Max. Processing Temp.	Ref.
NdFeB	BJT *1	3000	9000	150 °C	[31]
NdFeB	L-PBF	5900	8734	900 °C	[32]
NdFeB	FFF *4	690	5190	525 °C	[33]
NdFeB + SmFeN	BAAM *2	2800 - 11000	10800 - 11100	204 °C	[34]
NdFeB-Al	CS *3	4900	11000	800 °C	[35]
Ferrites	FFF	2200	3530	300 °C	[36]
$SmCo_5$	FFF	880	8970	160 °C	[37]
AlNiCo 8	DED *5	9200	1850	1250 °C	[38]
AlNiCo 9	DED	7200	1600	1215 °C	[39]

*1 (BJT): Binder Jetting, *2 (BAAM): Big Area Additive Manufacturing, *3 (CS): Cold Spray
*5 (ded): Directed Energy Deposition.

In summary, using the high flexibility of AM along with advanced material engineering, unconventional design solutions can be achieved. The main aim of this study is to assess the potential of 3D printing technology for high performance soft magnetic materials. Due to its flexibility towards material compositions, the micro-extrusion technique was used to print soft magnetic parts. This technology can also be used to print complex shapes which is impossible to achieve using traditional manufacturing techniques.

3. Material Morphology and Process Parameters

FeSi powders with 3wt% (Fe3Si, Sandvik Osprey) and 6.5wt% of Si (Fe6.5Si, Sandvik Osprey) were selected for the feedstock paste preparation. The powder's morphology was examined using scanning electron microscopy (SEM, XL30 FEI), and its Particle Size Distribution (PSD) was determined using a LS 13 320 particle size analyzer (Beckman Coulter™). **Fig. 4** (a,b) shows SEM images of the Fe3Si and Fe6.5Si powder respectively. The majority of the powder consisted of spherical particles, although a few elongated particles were also present. Additionally, smaller particles exhibited fine satellites on their surfaces. The PSD analysis for the Fe3Si grade resulted in 5.69 µm, 20.42 µm, and 43.42 µm for d10, d50, and d90, respectively. Similarly, the Fe6.5Si powder exhibited 4.19 µm, 17.47 µm, and 39.04 µm for d10, d50, and d90, respectively.

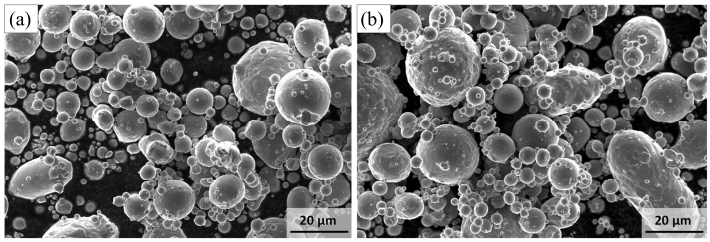

Fig. 4. SEM images of Fe3Si (a) and Fe6.5Si (b) powder employed for 3D micro-extrusion.

The technique of 3D micro-extrusion for FeSi involves extruding the material at room temperature, resulting in low energy consumption, making it an energy-saving process [40]. The feedstock material used in 3D micro-extrusion is a viscous highly powder-loaded paste, allowing for precise shaping. An advantage of this technique is that it does not require cleaning procedures after printing, eliminating the need for post-processing steps to remove internal cavities. However, an organic binder is necessary to hold the powder together during printing. The powder quality and particle sizes are carefully controlled with high resolution. The build rates for 3D micro-extrusion typically range from 10 to 100 cm^3/h, but larger printers can achieve rates up to 250 cm^3/h [41]. After printing, sintering in a furnace with a controlled atmosphere is commonly employed as a post-processing step. Furthermore, the use of multi-nozzle printers enables the possibility of multi-material printing. This technique excels in printing small details and thin walls, making it suitable for producing intricate components, and it offers a broad range of materials for fabrication.

4. Formulation and Testing Approaches

To measure the magnetic characteristics for a soft magnetic material, a two coil approach is commonly used. Moreover, according to the sample shape and dimensions, different test devices can be used [42]. For instance, if steel strips are to be measured, an Epstein frame will be the best approach [43]. Single sheet tester can also be used to test a single strip of the material. Normally, it consists of two u-shape yokes to have a closed magnetic circuit [44].

4.1. Testing 3D Printed Ring Core

Unlike other tools, a ring core is considered the best approach which can provide a mutual magnetic path for both primary and secondary coils without any airgap [45]. **Fig. 5** introduces the layout of the magnetic measurements using a two coil ring core. As can be seen, an AC input source is used as with a variable voltage and variable frequency to provide excitation for the primary coil. The flux then travels through the closed magnetic circuit and links the secondary coil. The induced voltage in the secondary coil is then measured using a voltage sensor. The data acquisition

system is then used to integrate this voltage signal to obtain waveform of the time-dependent magnetic flux density. By incorporating the waveforms of $B(t)$ and $H(t)$, the hysteresis loop can be instantaneously monitored at any excitation level. Furthermore, the system can also detect any DC offset and compensate it, because this undesired DC offset in the secondary voltage will create a significant rising ramp in the flux density waveform after the voltage waveform is integrated.

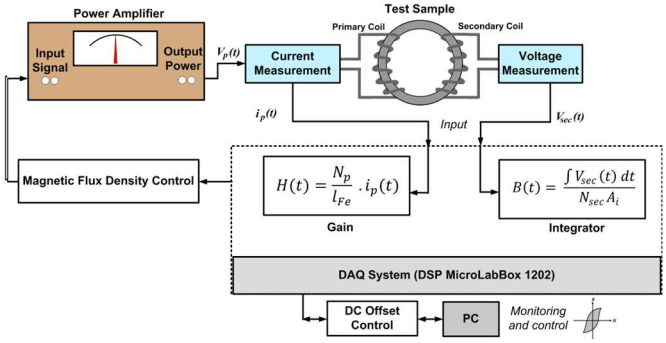

Fig. 5. Layout of the magnetic measurement of a ring core.

The magnetic properties of the soft magnetic material are evaluated by measuring the field strength $H(t)$ and the flux density $B(t)$ at the same time. Unlike SSTs, with the airgap absence, no calibration is needed and the field strength can estimated directly from the measured primary winding current $i_p(t)$ as follows :

$$H(t) = \frac{N_p}{l_m} . i_p(t) \tag{1}$$

where, $i_p(t)$ is the measured primary winding current, N_p is the number of its turns, and l_m is the mean value of magnetic path length. By integration of the induced back EMF in the secondary coil, the time varying magnetic flux density is obtained as follows.

$$B(t) = \frac{1}{N_{sec} A_{Fe}} \int V_{Sec}(t)\, dt \tag{2}$$

where, N_{sec} is the number of turns in the secondary, A_{Fe} is the core cross-section area of the ring core.

The flux linkage is obtained by a surface integral of the area inside the coil as follows.

$$\lambda = N_{sec} \int B\, dA \tag{3}$$

Moreover, the mean specific core loss in W/kg is calculated from the measured BH loop, during a single period of the fundamental frequency f as expressed bellow.

$$P_{core} = \frac{f}{\rho} \int_0^{1/f} H(t)\, \frac{dB(t)}{dt}\, dt \tag{4}$$

$$P_{core} = \frac{N_p\, f}{N_{sec}\, A_{Fe}\, l_m\, \rho} \int_0^{1/f} i_p(t)\, V_{sec}(t)\, dt \tag{5}$$

where ρ is the mass density of the soft magnetic material in kg/m3.

The total mass of the core (M) is the multiplication of the mass density (ρ) and the volume. In case of a uniform cross section area, the total mass of the core can be obtained as follows.

$$M = \rho\ A_{Fe} \frac{\pi(D_o + D_i)}{2} \tag{6}$$

It should be mentioned that the mean magnetic path length (l_m) is determined from this formula $\pi(D_o + D_i)/2$. Where D_o, $D_i$are the ring's outer and inner diameters, respectively. But, this is only applicable if the magnetic field is uniform over the cross-section area. In a nonuniform magnetic field, the magnetic path length should be calculated from the following equation [46]:

$$l_m = \frac{\pi(D_o - D_i)}{ln\,(\frac{D_o}{D_i})} \tag{7}$$

4.2. Testing 3D Printed Strips Using Single Sheet Tester

Since most of the AM techniques are still in experimental stage. Magnetic materials are only printed in rather small dimensions on laboratory scale. Single sheet testers (SSTs) are usually used for small strips in situations where there is no sufficient material for a standard Epstein frame (sample size 30mm x 280 mm).

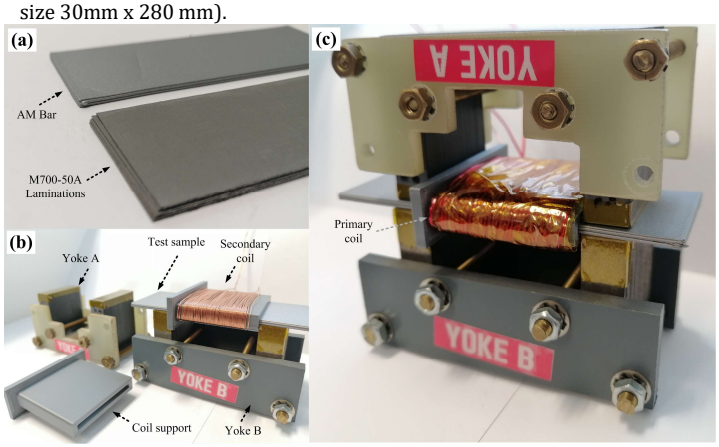

Fig. 6. custom-made single sheet tester (SST) for magnetic material characterization of rectangular strips. (a) Test samples. (b) SST components. (c) SST assembly.

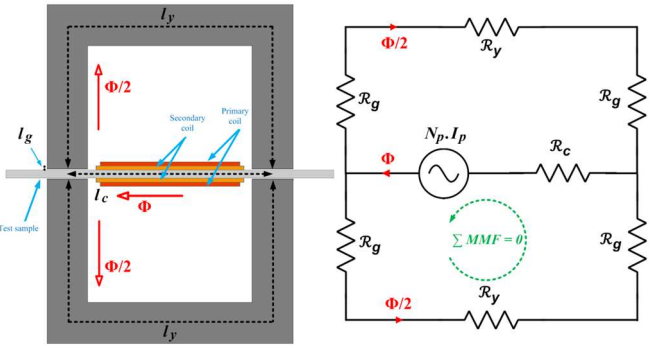

Fig. 7. Magnetic equivalent circuit model of the used single sheet tester.

Table 3. Magnetic Circuit Parameters.

Parameter	Symbol	Equation
Test core reluctance	$\mathcal{R}_c$	(8)
Yoke reluctance	$\mathcal{R}_y$	(9)
Airgap reluctance	$\mathcal{R}_g$	(10)
Test core mean magnetic path length	l_c	(8)
Yoke mean magnetic path length	l_y	(9)
Airgap length	l_g	(10)
Test core cross section area (fixed value)	A_c	(8)
Yoke cross section area (fixed value)	A_y	(9)
Airgap area	A_g	(10)
Magnetic flux in the sample	Φ	(12)(13)(14)
Magnetomotive Force	MMF	(15)

In order to measure the magnetic properties of the rectangular samples in this work, a custom-made SST is built and calibrated as shown in **Fig. 6**. Basically, it consists of two identical yokes facing each other to have a closed magnetic circuit for the test sample. The corresponding magnetic equivalent circuit is shown in **Fig. 7** and the definitions of all model components are listed in **Table 3**. The reluctances can be estimated based on the dimensions of the SST and the test sample as given by:

$$\mathcal{R}_c = \frac{1}{\mu_o \mu_c} \frac{l_c}{A_c} \tag{8}$$

$$\mathcal{R}_y = \frac{1}{\mu_o \mu_y} \frac{l_y}{A_y} \quad (9)$$

$$\mathcal{R}_g = \frac{1}{\mu_o} \frac{l_g}{A_g} \quad (10)$$

One major issue of the SST is the presence of airgap in the magnetic path length. Unlike Epstein frame, this is not automatically compensated. In SST, although the yoke cross section area (A_y) is fixed, the airgap area (A_g) does not have a constant value. The airgap width and area change as the flux density changes in the test sample. An example is demonstrated in **Fig. 8** for a FEM of the SST at 10Hz. It is noticed that the effective airgap area decreases as the maximum flux density of the sample increases.

The calibration procedures are carried out using the non-oriented electrical steel (grade M700-50A). Typically, these 0.50mm-laminations has a power loss of 4.66 W/kg at a magnetic induction of 1.5 T and a frequency of 50 Hz. The magnetic properties of these punched stripes are measured using a setup with Epstein frame in a range of frequency between 1 to 400 Hz, and maximum magnetic flux density between 0.1 to 1.6 T. The output results are then used as a reference for the calibration of the SST. The calibration process is made by comparing the measured core losses (i.e. obtained from the SST) to the reference values (i.e. from the Epstein frame).

Under different induction level (B) and frequencies (f), the effective airgap width and area are estimated so that the measured core loss corresponds to the reference value under the same conditions. **Fig. 9** shows the calibrated airgap width as function of magnetic flux density at different frequencies. It is noticed that the effective air gap width is highly impacted by the induction level (B). Also, high frequencies can reduce the effective airgap width only at low induction levels. At high induction levels, the frequency has a limited effect. Finally, these values of the effective air gap width are used in later measurements of magnetic properties of new samples.

Measuring the magnetic properties of a material requires measuring the field strength H(t) and the magnetic flux density B(t) simultaneously. The 3D printed rectangular bar is tested using the calibrated SST. The time varying magnetic flux density can be obtained by the integration of the back EMF induced into the secondary coil which have a number of turns of N_{sec}.

$$B_c(t) = \frac{1}{N_{sec} A_c} \int V_{Sec}(t)\, dt \quad (11)$$

Also, the magnetic flux can be estimated according to the cross section area of the test sample (A_c), as follows.

$$\Phi = B_c \,.\, A_c \quad (12)$$

Accordingly, the magnetic flux density in both of the yoke and the airgap (B_y , B_g) as well as the field intensity (H_y , H_g) can be estimated based on the calibrated airgap area (A_g) as follows.

$$B_y = \frac{\Phi/2}{A_y} \,, H_y = \frac{B_y}{\mu_o \mu_y} \quad (13)$$

$$B_g = \frac{\Phi/2}{A_g} \,, H_g = \frac{B_g}{\mu_o} \quad (14)$$

Then, the magnetic field intensity of the sample (H_c) is evaluated by calculating the MMF drop across each component on a closed loop (highlighted in green in **Fig. 7**).

$$\sum MMF = 0 \quad (15)$$

$$N_p I_p = H_c l_c + H_y l_y + 2 H_g l_g \quad (16)$$

$$H_c = \frac{1}{l_c} (N_p I_p - H_y l_y - 2 H_g l_g) \quad (17)$$

Where, N_p is the number of turns in the primary winding and l_c is the average magnetic path length of the test sample.

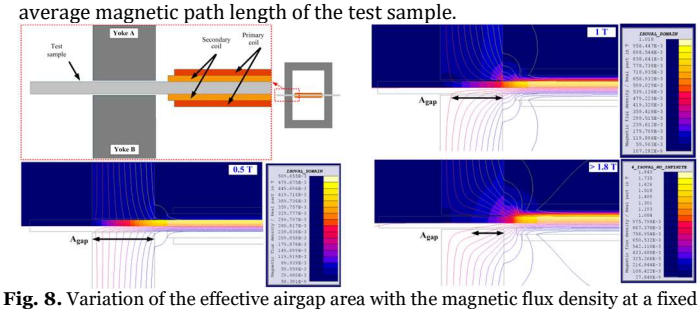

Fig. 8. Variation of the effective airgap area with the magnetic flux density at a fixed frequency of 10 Hz.

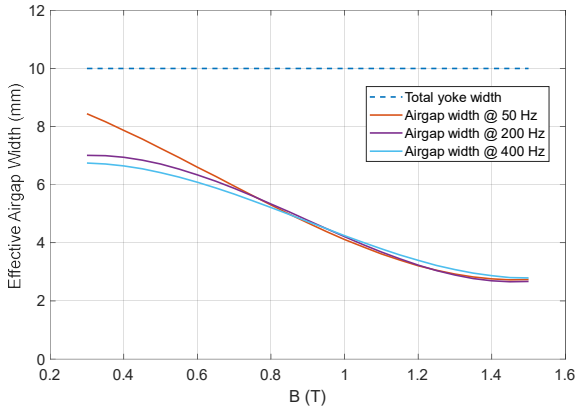

Fig. 9. The calibrated effective airgap width as a function of magnetic induction level at different frequency levels.

4.3. Sample Printing and Preparation

The 3D micro-extrusion technology has been employed to print ring core samples based on Fe-3Si and Fe-6Si powders. The powder materials are mixed with solvent, organic binder and stabilizing additives to produce a highly viscous powder-loaded paste. The paste is loaded into a syringe that is mounted on a nScrypt 3D printing machine. Extrusion of the paste through a thin nozzle (diameter 580µm for all samples apart from Hilbert sample with 840µm diameter nozzle) is performed at room temperature. Optimized printing parameters (scan spacing between neighboring extrusion lines, scan speed, mass low rate) resulting in a dense material are applied. Two cores are printed with the same outer and inner diameters utilizing the two different pastes. After printing, the green parts are thermally debinded and sintered under a controlled atmosphere of Ar and H2 to avoid the formation of oxides. The thermal cycle is shown in **Fig. 10**. As can be seen, both cores are first slowly heated to 500°C to remove the organic material. Then, sintering is performed at 1350°C during two hours to obtain a dense and strong steel. Finally, the material is cooled by furnace cooling to room temperature under the same atmosphere. The final sintered printed samples are shown in **Fig. 11**(a) and their specifications are listed in **Table 4**. In another experiment, a different heat treatment process is used for ring samples. An additional target of using controlled atmosphere is to allow for a naturally formed insulation layer without affecting the magnetic properties. After heat treatment, a naturally formed insulation layer is created due to the surface oxidation of a magnetic material (shown in black color in **Fig. 11**,b). This insulation layer is typically composed of iron oxide (Fe3O4), which prevents direct contact between ring laminations, and limiting the formation of eddy currents within the material. The electromagnetic performance of this sample is evaluated. Despite the higher surface resistance, the core losses results of this self-coating sample are nearly identical with the non-oxidized samples. Yet, the only issue is that this process results in a lower mechanical fixability. Consequently, thin laminations subjected to excessive forces may be susceptible to breakage. Furthermore, to ensure complete and reliable insulation, an additional measure of applying a varnish coating is employed. This varnish coating further enhances the insulation properties by perfectly isolating all laminations, leaving no room for potential electrical contact and ensuring

optimal performance of the magnetic sample.

To measure the magnetic characteristics, primary and secondary coils are placed around the ring cores, as shown in **Fig. 12**. It is important to have different sets of coils around the ring core. For instance, at very low frequency levels, the secondary coil should have a very high number of turns to be able to detect very small voltages. While at high frequency, only few turns can be sufficient.

Table 4. Specifications of the ring core samples utilized for magnetic testing.

Sample	Fe-3Si bar	Fe-3Si ring	Fe-6Si ring
Silicon content	3 wt%	3 wt%	6 wt%
Outer diameters	-	55.6	56.7
Inner diameters	-	39.3 mm	42mm
Dimensions	30mm x 80 mm	-	-
Heat treatment	1400°C (pure H_2)	1350°C (Ar + H_2)	1350°C (Ar + H_2)
AM technology	3D micro extrusion	3D micro extrusion	3D micro extrusion

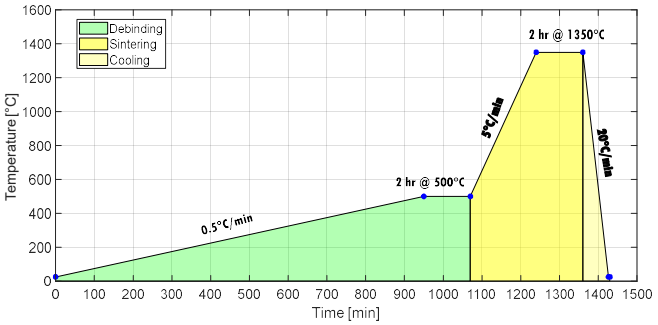

Fig. 10. Thermal post-processing applied to the printed Fe-Si samples.

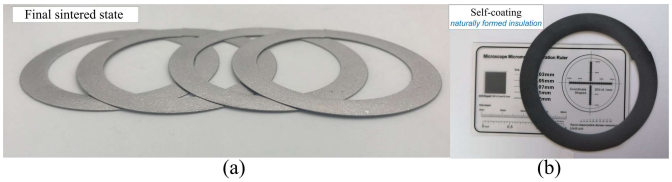

Fig. 11. 3D micro-extruded Fe-Si ring cores. (a) Final sintered state, (b) Self-coating.

Fig. 12. Preparing the test sample with the measurement coils. (a) Fe-3Si, (b) Fe-6Si.

5. Material Characterization of the 3D-printed Fe-Si parts

5.1. Test Setup and Offset Control

The core losses are measured at different frequency levels (10,20,50, and 100Hz) using the test setup in **Fig. 13**. The main specifications are listed in **Table 5**. A variable AC voltage source is used with a maximum input power 10 kVA. This amplifier can provide an excitation for the primary coil up to 40A and 270 V. Additionally, the input source offers a variable input frequency range starting from very low frequencies of 1 Hz up to very high frequencies of 10 kHz. Furthermore, current and voltage sensors are used to detect the primary current and the secondary voltage. These signals are then injected into a data acquisition system (DAQ) which is a 1202 MicroLabBox. The DAQ is also used to integrate the secondary voltage waveform to obtain the flux density waveform. The test core is connected in series with a high rating resistance with zero inductance. This resistance is useful to keep a sinusoidal current especially at high frequencies.

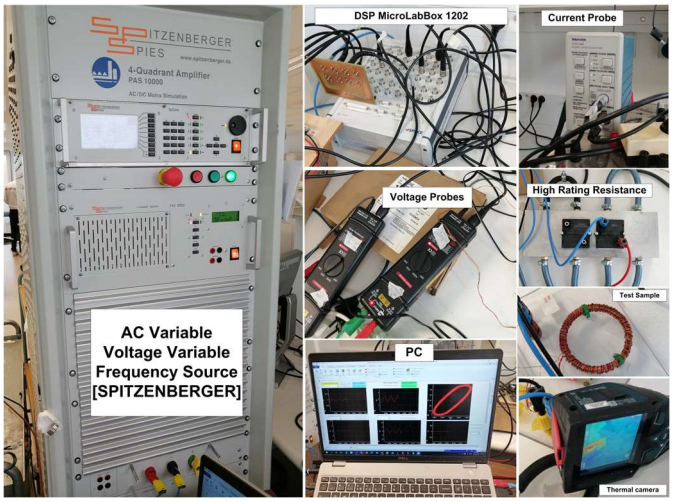

Fig. 13. Test platform for magnetic material measurements.

Table 5. Test setup specifications.

Specifications	Value
Input power range	1–25 kVA
Frequency range	1 Hz– 10 kHz
Data acquisition card model	dSP MicroLabBox 1202
Secondary voltage limits	±200 V
Sampling time	1×10^{-5}
Input source & Model type	Spitzenberger (PAS 10,000)
Peak output power	10,000 VA
Max. input voltage & input current	270 V, 40 A
Voltage probe / Differential probes	DP25 DC-25Mhz V, 1000V
Current probe	Tektronix, TCP305A (5 mA - 50 A)

The secondary voltage, displayed in **Fig. 14**, is measured. It is observed that the sinusoidal voltage waveform exhibits a small DC offset. The presence of this unwanted offset poses a significant issue as it results in a continuously rising ramp function in the flux density waveform following the integration of the secondary voltage. Consequently, it becomes imperative to eliminate this minor DC offset. **Fig. 15** provides a comparison of the magnetic flux density waveform before and after offset control, clearly demonstrating the removal of the ramp function and the prevention of illogical values in the flux density. Similarly, **Fig. 16** presents a comparison of the BH loops, indicating that after DC offset control, all BH loops exhibit almost identical characteristics under the same field intensity. This significant improvement in accuracy ensures highly reliable measurement results.

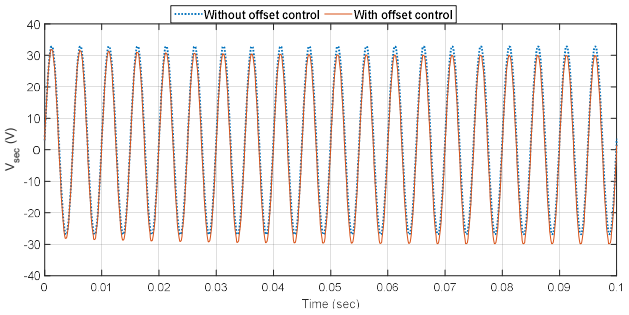

Fig. 14. Measured secondary voltage with and without offset control.

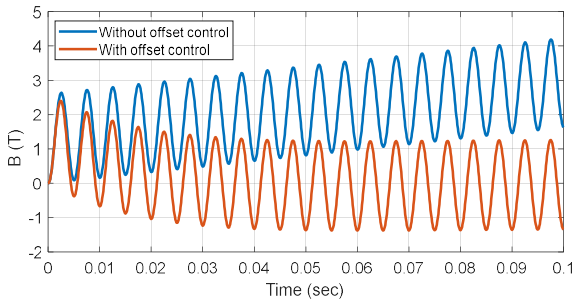

Fig. 15. Measured magnetic flux density with and without offset control.

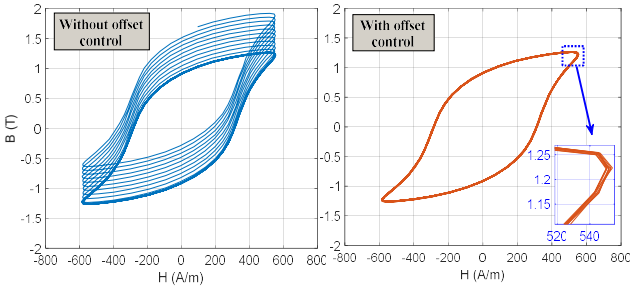

Fig. 16. BH loop with and without offset control.

5.2. Core Loss Measurements

First, the SST samples are compared after calibration at 50Hz as shown in **Fig. 17**(a). Interestingly, the 3D Fe-3%Si printed bar has lower core losses than the standard M700-50A. The core loss results at 50 Hz of both ring cores are compared in **Fig. 17**(b), revealing that the Fe-3Si ring core has ≥140% higher losses than the Fe-6Si ring. The single valued BH curves are compared at the same frequency in **Fig. 18**(a).). Obviously, the Fe-6Si ring core can reach a higher magnetic induction. Moreover, the measured BH loops are compared at the same conditions of frequency and magnetic flux density in **Fig. 18**(b). Obviously, the larger loop of the Fe-3Si ring core gives an indication of the higher losses. Finally, the Fe-6Si alloy is recommended for higher magnetic flux values.

5.3. BH Curve Modeling

The three parameter model is commonly used to link the measured BH curve properties with FEM simulations. Using the measurement results, the single valued BH curve can be modeled using the following three parameter relation as shown in **Fig. 19**.

$$\frac{H}{H_o} = \frac{B}{B_o} + \left(\frac{B}{B_o}\right)^{v} \tag{18}$$

where, B_o, H_o, v are the three fixed parameters used to fit the measurement data. The results of these fitting parameters are listed in **Table 6**. From (18), the relative permeability can be obtained as follows.

$$\mu_r = \frac{B_o}{H_o \mu_o \left[1 + \left(\frac{B}{B_o}\right)^{v-1}\right]} \tag{19}$$

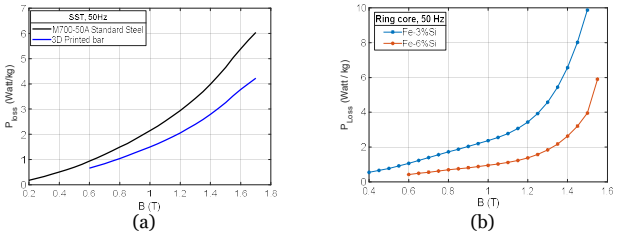

Fig. 17. Measurements of the core losses for the different 3D printed Fe-Si samples at 50 Hz. (a) Single sheet tester. (b) Ring cores with different Si content.

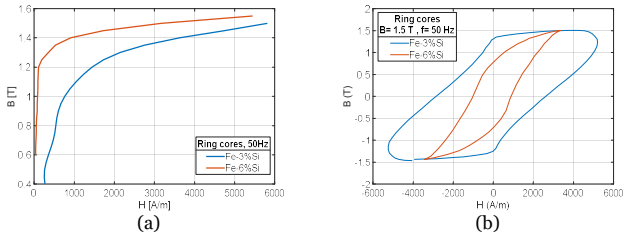

Fig. 18. Comparison between the Fe-3Si and the Fe-6Si ring cores at 50 Hz. (a) Normalized BH curve. (b) Measured BH loop at 1.5T.

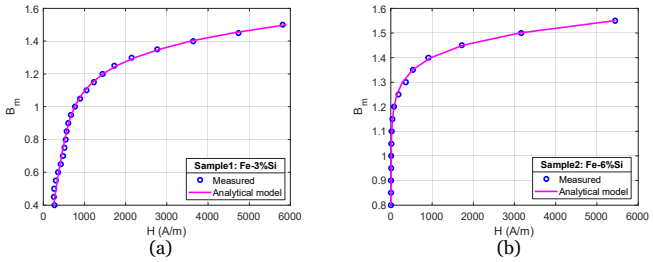

Fig. 19. BH curve fitting using the three parameter relation. (a) Fe-3Si ring, (b) Fe-6Si ring

Table 6. Three fitting parameters for the single valued BH relation.

Samples	Si content	B_o	H_o	v
Fe-3Si ring	3%	1.2106	755.719	8.786
Fe-6Si ring	6%	0.96467	172.757	16.9883

5.4. Core Losses Fitting

Based on the principle of the losses separation, core losses can be divided into three main components as indicated in the following equation.

$$P_{core} = P_h + P_{cl} + P_{exc} \tag{20}$$

Where Ph is the hysteresis losses, Pcl is the classical eddy current, and Pexc is the excess losses. Each component is a function of the magnetic flux density (B_m) and the frequency (f). A 6-parameter model is used to characterize the measured specific core losses of the test samples as follows.

$$P_{core} = K_h f B_m^{\alpha_1} + K_{cl}(f B_m)^{\alpha_2} + K_{exc}(f B_m)^{\alpha_3} \tag{21}$$

Where K_h, K_{cl}, K_{exc}, $\alpha_1, \alpha_2, \alpha_3$ are the fitting parameters as descripted in **Table 7**. Using an inverse problem approach, these parameters are evaluated for both cores and the results are compared in **Fig. 20**. A good agreement is obtained at different magnetic flux densities.

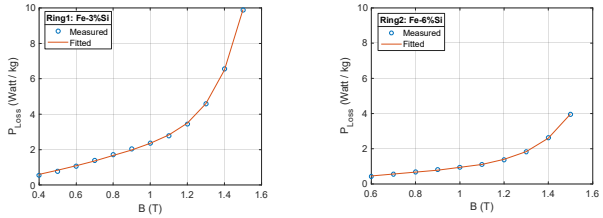

Fig. 20. Core loss fitting using separation principle. (a) Fe-3Si ring, (b) Fe-6Si ring.

Table 7. Three fitting parameters for the single valued BH relation.

Coefficient	Symbol	Fe-3Si ring	Fe-6Si ring
Hysteresis losses coefficient	K_h	1.310705 * 10^{-3}	7.81675* 10^{-4}
Classical losses coefficient	K_{cl}	4.482250 * 10^{-8}	1.20767* 10^{-4}
Excess losses coefficient	K_{exc}	6.984553 * 10^{-3}	5.24764* 10^{-3}
Hysteresis losses exponent	α_1	11.017	10.164
Classical losses exponent	α_2	2.2	1.745
Excess losses exponent	α_3	1.483	1.280

6. Advanced Shape Profiled Cores

After the best Fe-Si material is identified and the measured magnetic properties are linked to the FEM simulations, different shapes are investigated targeting minimized eddy current losses as shown in **Fig. 21**. The cross section shapes are selected based on the approach of space-filling curves [47]. The initial simulation is done for all four shapes using two separate cores symmetrical around y-axis indicated in the figure. The same coil design is used around the core to produce flux in the z-direction. It is found that the clock spring and Hilbert shapes can reduce the high frequency eddy currents compared to the solid core or the parallel plates one. That is why these two shapes are then printed using the same technology and the same powder material.

Using 3D micro extrusion, two identical cores are printed for two different shapes of the clock spring and the Hilbert shape as shown in **Fig. 22**. For a fair comparison between both shapes, Fe-6Si is used for the chemical composition of the powder and the same thermal treatment process is used. It should be mentioned that a lot of trials have been made to get a uniform shrinkage. Deformation caused by non-uniform shrinkage after heat treatment is a common challenge encountered in materials processing. During sintering, differential contraction across a material can lead to uneven shrinkage, resulting in undesirable deformations and dimensional inconsistencies.

To achieve uniform shrinkage, several solutions have been explored. One approach involves optimizing the heat treatment cycle, including preheating, soaking stages, and atmosphere, to promote controlled and uniform contraction throughout the material. Another strategy is the incorporation of a support plate underneath the material during heat treatment. By providing a stable foundation, the support plate helps to guide the shrinkage and maintain dimensional accuracy. The use of a support plate in the design base offers a practical solution to address non-uniform shrinkage, reducing the deformation and ensuring more consistent final dimensions in the heat-treated part. This strategy was only employed for the clock spring sample, as this design encountered more issues with non-uniform shrinkage.

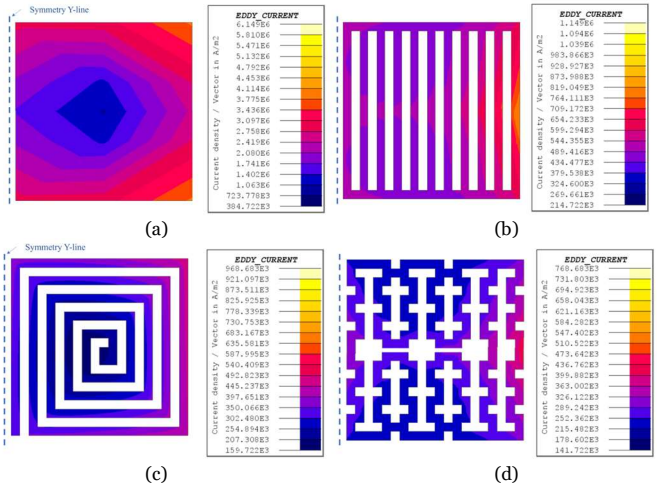

Fig. 21. Eddy currents at 1.5 T and 100 Hz. (a) Solid core, (b) Parallel plates, (c) Clock spring, (d) Hilbert shape.

To measure the magnetic properties of the printed cores, a custom-made tester is manufactured specifically with two facing U-shape cores as shown in **Fig. 23**. Also, a compression unit is assembled with the SST to investigate the impact of mechanical stress on the magnetic properties. Furthermore, blocks of standard electrical laminated steel are used to calibrate the tester as shown in **Fig. 24** using the same approach in Section 3.2. The results for M700-50A after calibration are shown in **Fig. 25** at different frequency levels. The measured losses have a very high agreement with the datasheet losses.

The magnetic properties of the printed cores are evaluated at 100Hz and the results are compared with standard electrical steel of different grades such as NO20 and M700-50A. The BH cures are compared in **Fig. 26** without applying any mechanical stress. It is clear that the magnetization curve of the Hilbert shape is relatively better than the clock spring especially near saturation levels. Furthermore, the specific core losses are measured and compared at 100Hz as shown in **Fig. 27**. Obviously, the Hilbert shape has much lower losses compared to the clock spring. The Hilbert shape has also better performance than the M700-50A despite having the same wall thickness. Still, the Hilbert shape has higher losses compared to the NO20 under stress-free conditions. Yet, with thinner wall thickness, the Hilbert shape is expected to provide very comparable losses.

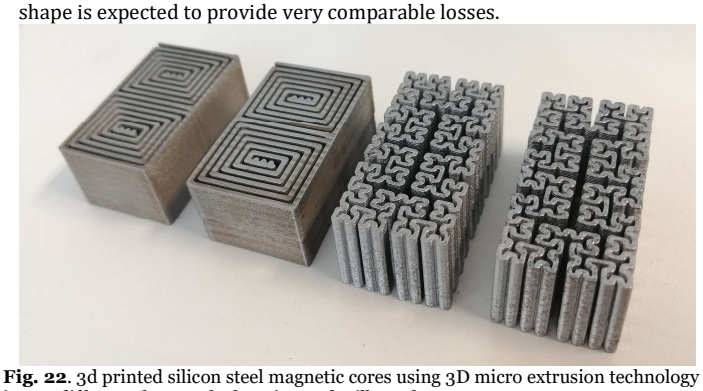

Fig. 22. 3d printed silicon steel magnetic cores using 3D micro extrusion technology in two different shapes: clock spring and Hilbert shapes.

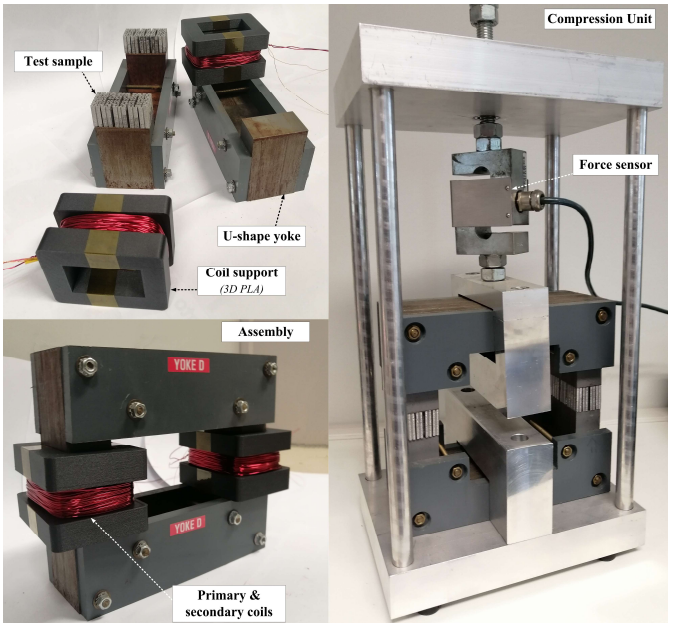

Fig. 23. Custom-made U-shape tester for testing magnetic blocks and assembly with a compression unit.

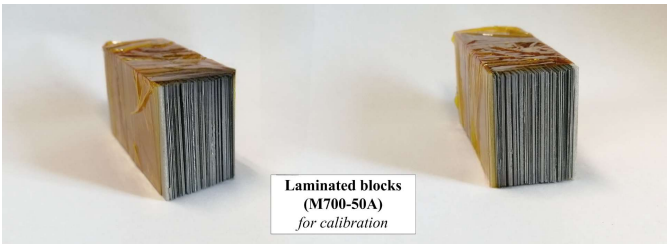

Fig. 24. Blocks of standard laminated electrical steel for the calibration of the U-shape tester.

Finally, the effect of external compression is investigated by applying mechanical stress during the magnetic measurements. In **Fig. 28** illustrates the core losses at 1.5T and 100Hz, measured under various compressive forces ranging from stress-free conditions up to 120 MPa. The results clearly demonstrate a significant increase in core losses for conventional laminations as the stress level rises. Conversely, the core losses in the 3D

printed cores exhibit a more gradual increase compared to the conventional laminations. This implies that the 3D printed cores are more resilient to higher levels of stress. Specifically, when subjected to compressive forces starting from 60 MPa, the Hilbert-shaped cores exhibit lower losses compared to the NO20 cores. Moreover, above 85 MPa, the clock spring core outperforms the M700-50A core in terms of losses. To summarize, the findings indicate that 3D printed cores can withstand higher mechanical stress levels in comparison to standard steel laminations.

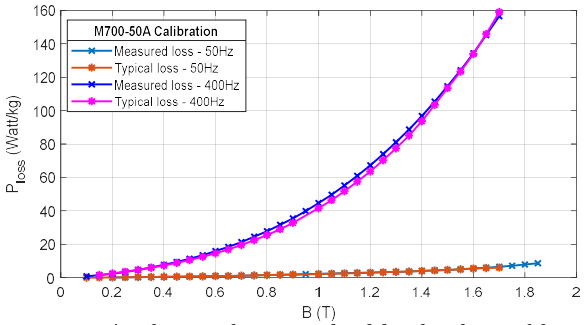

Fig. 25. Comparison between the measured and datasheet losses of the standard M700-50A electrical steel after calibration of the U-shape tester.

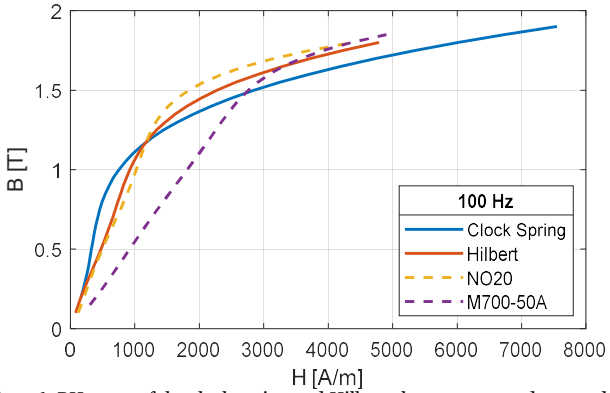

Fig. 26. BH curve of the clock spring and Hilbert shapes compared to standard steel.

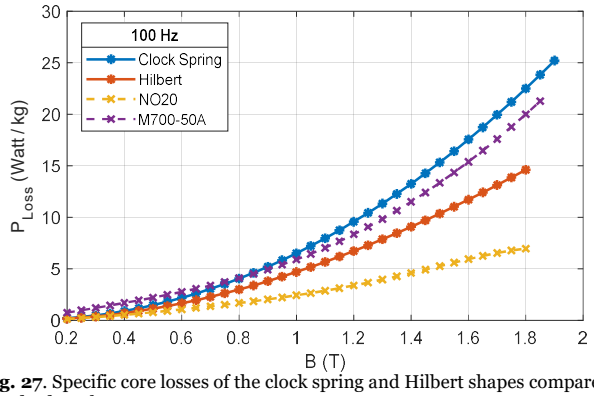

Fig. 27. Specific core losses of the clock spring and Hilbert shapes compared to standard steel at 100Hz.

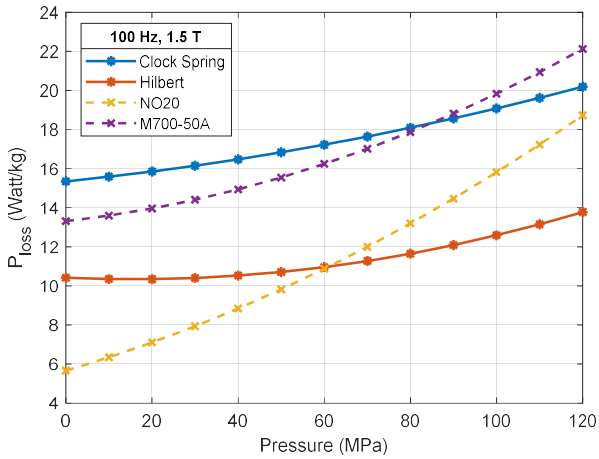

Fig. 28. Effect of compression on the core losses of the clock spring and Hilbert shapes compared to standard steel at 100Hz.

7. Conclusions

Using 3D micro extrusion AM technology, different soft magnetic Fe-Si alloy samples with 3 and 6 wt% Si were printed. The test samples are printed and subsequently thermal treated to remove organic material by thermal debinding and to densify the powder by sintering at high temperature. The magnetic properties of 3D printed samples were measured and compared using different approached such as ring cores and SST. The Fe-3Si bar has relatively lower losses than the standard M700-50A electrical steel. The Fe-6Si ring core reached a high magnetic flux density with remarkably lower losses than the Fe-3Si ring core. The measurement results were modelled to generate the fitting parameters which can be used for finite element simulations of magnetic material parts. Furthermore, advanced shape profiled cores are investigated for lower eddy current losses. Two shapes have been selected for the printing process which are Hilbert and clock spring shapes. The magnetic properties of the prototyped cores are measured and compared with the typical electrical steel. It is concluded that the Hilbert shape has very comparable magnetic properties with the standard magnetic materials. Under external mechanical stress, the 3D printed parts are less affected by compressive forces resulting in lower core losses compared to conventional laminations. This research highlights the growing importance and the ability of additive manufacturing to control and adjust the material composition of soft materials to build loss-mitigating complex shapes core structures which can enable higher performance electrical machines.

Declaration of Competing Interests

The authors declare that they have no known competing interests that influences the work reported in this paper.

Acknowledgements

This research is financially supported by the Research Foundation—Flanders (FWO) in the project (S001721N) entitled Multi-Material Additive Manufacturing for Electrical Machines with increased performance (AM4EM).

References

[1] Punch-Powertrain-NV;, Optimized E-Motors - Punch Powertrain NV, (2023). https://punchpowertrain.com/products/e-motors/ (accessed March 11, 2023).

[2] S. Darius Gnanaraj, E. Gundabattini, R. Raja Singh, Materials for lightweight electric motors – a review, IOP Conf. Ser. Mater. Sci. Eng. 906 (2020) 012020. https://doi.org/10.1088/1757-899X/906/1/012020.

[3] A. Selema, M.N. Ibrahim, H. Vansompel, P. Sergeant, Development of Yokeless Axial Flux Machine Using 3D-Printed Shape-Profiled Core, in: 2022 Int. Conf. Electr. Mach., IEEE, Valencia, Spain, 2022.

[4] A. Selema, M.N. Ibrahim, P. Sergeant, Additively Manufactured Ultralight Shaped-Profile Windings for HF Electrical Machines and Weight-Sensitive Applications, IEEE Trans. Transp. Electrif. 8 (2022) 4313–4324. https://doi.org/10.1109/TTE.2022.3173126.

[5] A. Selema, M.N. Ibrahim, P. Sergeant, Development of Novel Semi-Stranded Windings for High Speed Electrical Machines Enabled by Additive Manufacturing, Appl. Sci. 13 (2023) 1653. https://doi.org/10.3390/app13031653.

[6] M. Beretta, S. Kolli, A. Selema, P. Sergeant, L.A.I. Kestens, M. Rombouts, J. Vleugels, Process optimization and characterization of dense pure copper parts produced by paste-based 3D micro-extrusion, Addit. Manuf. (2023) 103670. https://doi.org/10.1016/j.addma.2023.103670.

[7] A. Selema, M.N. Ibrahim, P. Sergeant, Electrical Machines Winding Technology: Latest Advancements For Transportation Electrification, Machines. 10 (2022).

[8] A. Selema, M.N. Ibrahim, P. Sergeant, Mitigation of High-Frequency Eddy Current Losses in Hairpin Winding Machines, Machines. 10 (2022) 328. https://doi.org/10.3390/machines10050328.

[9] A. Selema, M. Gulec, M.N. Ibrahim, R. Sprangers, P. Sergeant, Selection of Magnet Wire Topologies With Reduced AC Losses for the Windings of Electric Drivetrains, IEEE Access. 10 (2022) 121531–121546. https://doi.org/10.1109/ACCESS.2022.3222773.

[10] A. Selema, M. Van Coppenolle, M.N. Ibrahim, P. Sergeant, Multi-physic design of ultra-efficient smart motor enabled by additive manufacturing, Proc. Fac. Eng. Archit. Res. Symp. (2022). https://doi.org/10.5281/zenodo.7405841.

[11] S.J. Raab, R. Guschlbauer, M.A. Lodes, C. Körner, Thermal and Electrical Conductivity of 99.9% Pure Copper Processed via Selective Electron Beam Melting, Adv. Eng. Mater. 18 (2016) 1661–1666. https://doi.org/10.1002/adem.201600078.

[12] D.D. Lima, S.A. Mantri, C. V. Mikler, R. Contieri, C.J. Yannetta, K.N. Campo, E.S. Lopes, M.J. Styles, T. Borkar, R. Caram, R. Banerjee, Laser additive processing of a functionally graded internal fracture fixation plate, Mater. Des. 130 (2017) 8–15. https://doi.org/10.1016/J.MATDES.2017.05.034.

[13] E. Peng, X. Wei, T.S. Herng, U. Garbe, D. Yu, J. Ding, Ferrite-based soft and hard magnetic structures by extrusion free-forming, RSC Adv. 7 (2017) 27128–27138. https://doi.org/10.1039/C7RA03251J.

[14] A. Selema, M. Beretta, M. Van Coppenolle, H. Tiismus, A. Kallaste, M. Ibrahim, M. Rombouts, J. Vleugels, L. Kestens, P. Sergeant, Evaluation of 3d-Printed Magnetic Materials for Additively-Manufactured Electrical Machines, J. Magn. Magn. Mater. (2023). https://doi.org/10.1016/j.jmmm.2023.170426.

[15] TUChemnitz; 3D-Multimaterialdruck, 3D multi-material printing, (2020). https://www.tu-chemnitz.de/etit/ema/AMMM/index.php (accessed February 10, 2023).

[16] T. Pham, P. Kwon, S. Foster, Additive Manufacturing and Topology Optimization of Magnetic Materials for Electrical Machines—A Review, Energies. 14 (2021) 283. https://doi.org/10.3390/en14020283.

[17] and R.M. Stornelli, Giulia, Antonio Faba, Andrea Di Schino, Paolo Folgarait, Maria Rita Ridolfi, Ermanno Cardelli, Properties of Additively Manufactured Electric Steel Powder Cores with Increased Si Content, Materials (Basel). 14 (2021). https://doi.org/10.3390/ma14061489.

[18] D. Goll, J. Schurr, F. Trauter, J. Schanz, T. Bernthaler, H. Riegel, G. Schneider, Additive manufacturing of soft and hard magnetic materials, Procedia CIRP. 94 (2020) 248–253. https://doi.org/10.1016/j.procir.2020.09.047.

[19] J.W.J. Bonuk Koo, Min-Sun Jang, Yeong Gyun Nam, Sangsun Yang, Jihun Yu, Yong Ho Park, Structurally-layered soft magnetic Fe-Si components with surface insulation prepared by shell-shaping selective laser melting, Appl. Surf. Sci. 553 (2021). https://doi.org/10.1016/j.apsusc.2021.149510.

[20] A. Hamler, V. Goričan, B. Šuštaršič, A. Sirc, The use of soft magnetic composite materials in synchronous electric motor, J. Magn. Magn. Mater. 304 (2006). https://doi.org/10.1016/J.JMMM.2006.03.003.

[21] J. Wegner, M. Frey, M. Piechotta, N. Neuber, B. Adam, S. Platt, L. Ruschel, N. Schnell, S.S. Riegler, H.R. Jiang, G. Witt, R. Busch, S. Kleszczynski, Influence of powder characteristics on the structural and the mechanical properties of additively manufactured Zr-based bulk metallic glass, Mater. Des. 209 (2021). https://doi.org/10.1016/j.matdes.2021.109976.

[22] E.A. Périgo, J. Jacimovic, F. García Ferré, L.M. Scherf, Additive manufacturing of magnetic materials, Addit. Manuf. 30 (2019). https://doi.org/10.1016/j.addma.2019.100870.

[23] L. Thorsson, M. Unosson, M. Teresa Pérez-Prado, X. Jin, P. Tiberto, G. Barrera, B. Adam, N. Neuber, A. Ghavimi, M. Frey, R. Busch, I. Gallino, Selective laser melting of a Fe-Si-Cr-B-C-based complex-shaped amorphous soft-magnetic electric motor rotor with record dimensions, Mater. Des. 215 (2022) 110483. https://doi.org/10.1016/J.MATDES.2022.110483.

[24] J.M. Silveyra, E. Ferrara, D.L. Huber, T.C. Monson, Soft magnetic materials for a sustainable and electrified world, Science (80-.). 362 (2018). https://doi.org/10.1126/SCIENCE.AAO0195.

[25] F. Nishanth, A.D. Goodall, I. Todd, E.L. Severson, Characterization of an Axial Flux Machine with an Additively Manufactured Stator, IEEE Trans. Energy Convers. (2023) 1–13. https://doi.org/10.1109/TEC.2023.3285539.

[26] Sandvik, Chemical composition of soft magnetic alloys, (2023). https://www.metalpowder.sandvik/en/products/metal-powder-alloys/soft-magnetic-alloys/ (accessed February 18, 2023).

[27] Sinotech, Custom Motor Laminations: Nickel & Cobalt Alloys, (2023). https://sinotech.com/blog/motor-laminations-nickel-cobalt-alloys/ (accessed March 13, 2023).

[28] D.S. Schmool, D. Markó, Magnetism in Solids: Hysteresis, in: Ref. Modul. Mater. Sci. Mater. Eng., Elsevier, 2018. https://doi.org/10.1016/B978-0-12-803581-8.11413-4.

[29] (ECHA)-European-Chemicals-Agency, European Chemicals Agency (ECHA), REACH, (2021). https://ec.europa.eu/environment/chemicals/reach/reach_en.htm (accessed March 14, 2023).

[30] Sciencedaily, Understanding cobalt's human cost, (2023). https://www.sciencedaily.com/releases/2021/12/211217113232.htm# (accessed March 10, 2023).

[31] M.P. Paranthaman, C.S. Shafer, A.M. Elliott, D.H. Siddel, M.A. McGuire, R.M. Springfield, J. Martin, R. Fredette, J. Ormerod, Binder Jetting: A Novel NdFeB Bonded Magnet Fabrication Process, JOM. 68 (2016) 1978–1982. https://doi.org/10.1007/s11837-016-1883-4.

[32] J. Jaćimović, F. Binda, L.G. Herrmann, F. Greuter, J. Genta, M. Calvo, T. Tomše, R.A. Simon, Net Shape 3D Printed NdFeB Permanent Magnet, Adv. Eng. Mater. 19 (2017) 1700098. https://doi.org/10.1002/adem.201700098.

[33] L. Pigliaru, M. Rinaldi, L. Ciccacci, A. Norman, T. Rohr, T. Ghidini, F. Nanni, 3D printing of high performance polymer-bonded PEEK-NdFeB magnetic composite materials, Funct. Compos. Mater. 1 (2020) 4. https://doi.org/10.1186/s42252-020-00006-w.

[34] K. Gandha, L. Li, I.C. Nlebedim, B.K. Post, V. Kunc, B.C. Sales, J. Bell, M.P. Paranthaman, Additive manufacturing of anisotropic hybrid NdFeB-SmFeN nylon composite bonded magnets, J. Magn. Magn. Mater. 467 (2018) 8–13. https://doi.org/10.1016/j.jmmm.2018.07.021.

[35] J.-M. Lamarre, F. Bernier, Permanent Magnets Produced by Cold Spray Additive Manufacturing for Electric Engines, J. Therm. Spray Technol. 28 (2019) 1709–1717. https://doi.org/10.1007/s11666-019-00917-6.

[36] K. Sonnleitner, C. Huber, I. Teliban, S. Kobe, B. Saje, D. Kagerbauer, M. Reissner, C. Lengauer, M. Groenefeld, D. Suess, 3D printing of polymer-bonded anisotropic magnets in an external magnetic field and by a modified production process, Appl. Phys. Lett. 116 (2020). https://doi.org/10.1063/1.5142692.

[37] H.A. Khazdozian, J.S. Manzano, K. Gandha, I.I. Slowing, I.C. Nlebedim, Recycled Sm-Co bonded magnet filaments for 3D printing of magnets, AIP Adv. 8 (2018) 056722. https://doi.org/10.1063/1.5007669.

[38] E.M.H. White, A.G. Kassen, E. Simsek, W. Tang, R.T. Ott, I.E. Anderson, Net Shape Processing of Alnico Magnets by Additive Manufacturing, IEEE Trans. Magn. 53 (2017) 1–6. https://doi.org/10.1109/TMAG.2017.2711965.

[39] E. White, E. Rinko, T. Prost, T. Horn, C. Ledford, C. Rock, I. Anderson, Processing of Alnico Magnets by Additive Manufacturing, Appl. Sci. 9 (2019) 4843. https://doi.org/10.3390/app9224843.

[40] D.A.G. to M.A. Manufacturing, Energy Consumption in Metal Additive Manufacturing, (2019). https://www.digitalalloys.com/blog/energy-consumption-metal-additive-manufacturing/ (accessed December 21, 2022).

[41] All3dp; Digital Maker Magazine, Selective Laser Melting Guide, (2021). https://all3dp.com/1/selective-laser-melting-guide/ (accessed December 21, 2022).

[42] A. Selema, M.N. Ibrahim, P. Sergeant, Non-Destructive Electromagnetic Evaluation of Material Degradation Due to Steel Cutting in a Fully Stacked Electrical Machine, Energies. 15 (2022) 7862. https://doi.org/10.3390/en15217862.

[43] A. International, Standard Test Method For Alternating-Current Magnetic Properties Of Materials At Power Frequencies Using Wattmeter-Ammeter-Voltmeter Method And 25-Cm Epstein Test Frame, (2022). https://webstore.ansi.org/Standards/ASTM/astma343a343m03 (accessed October 14, 2022).

[44] Y. Zhang, J. Zhao, L. Wang, Y. Guo, Z. Li, J. Huang, Optimization of Two-Dimensional Rotational Single Sheet Tester, in: 2019 22nd Int. Conf. Electr. Mach. Syst., IEEE, 2019: pp. 1–4. https://doi.org/10.1109/ICEMS.2019.8922126.

[45] A. Kahveci, P. Szary, F. Herget, A.K. Putri, K. Hameyer, Methods for hysteresis losses determinations at non-standard ring core geometries equivalent to Epstein

measurements, in: 2016 6th Int. Electr. Drives Prod. Conf., IEEE, 2016: pp. 135–142. https://doi.org/10.1109/EDPC.2016.7851325.

[46] A. Krings, J. Soulard, O. Wallmark, PWM Influence on the Iron Losses and Characteristics of a Slotless Permanent-Magnet Motor With SiFe and NiFe Stator Cores, IEEE Trans. Ind. Appl. 51 (2015) 1475–1484. https://doi.org/10.1109/TIA.2014.2354735.

[47] H. Sagan, Space-Filling Curves, Springer New York, New York, NY, 1994. https://doi.org/10.1007/978-1-4612-0871-6.